ACS MATERIALS LETTERS



www.acsmaterialsletters.org
Letter

# Nanoconfined Grain Boundaries Increase the Conductivity of Polycrystalline Molecular Crystals

Shujit Chandra Paul, William A. Goddard, III, Michael J. Zdilla,* Prabhat Prakash,* and Stephanie L. Wunder*

Cite This: ACS Materials Lett. 2026, 8, 764−771
Read Online

ACCESS | Metrics & More | Article Recommendations | Supporting Information

**ABSTRACT:** Soft-solid molecular crystals consist of crystalline grains and fluid grain boundaries (GBs) that enhance the grain binding and transport of $Li^+$ ions between the grains. The total ionic conductivity consists of ion migration in both the grains and GBs. To unravel these contributions in adiponitrile (Adpn):$LiPF_6$ molecular crystals, the GB volume fraction was varied by changing the size of the crystals and the Adpn:$LiPF_6$ molar ratio. Molecular dynamics (MD) simulations indicate that ion motion was subdiffusive in the grains and "well-diffusive" in the GBs, with GBs characterized as disordered nanoconfined regions of higher charge carrier concentration (∼1 M) than in saturated Adpn:$LiPF_6$ solutions (0.04 M), and $Li^+$ ions predominantly solvated by cyano groups with few contact ion pairs. The diffusivity in the GBs is at least an order of magnitude higher than that in the crystalline grains. The emergent picture is the grains as a reservoir of ions that migrate to faster-conducting GBs.

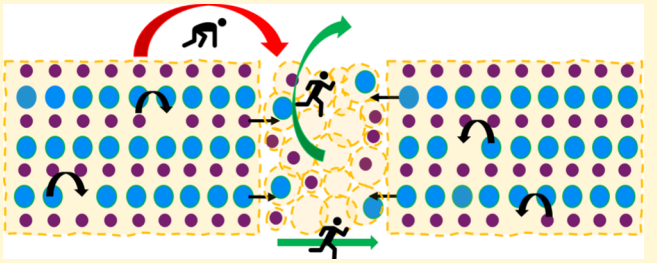



Solid electrolytes provide safety advantages over liquid electrolytes and have thus been investigated for use in Li metal (LMBs), lithium-ion (LIBs) batteries, and next-generation batteries. The solid electrolytes investigated have been inorganic lithium-ion conductive ceramics (LICCs),[1,2] polymer or polymer gel electrolytes,[3] or composite electrolytes with inorganic and organic components. LICCs can have conductivities greater than liquid electrolytes, but are brittle, with resistive grain boundaries,[4] while polymer electrolytes are flexible and malleable but have poor ionic conductivity, the latter of which can be enhanced by addition of liquids to form gels. Composite electrolytes were proposed to combine advantages of the LICCs and polymers.[5] However, there appears to be a barrier to $Li^+$ ion migration between the inorganic and organic phases, with the resistance at the interface limiting the total ionic conductivity.

Enhanced ionic conductivity in soft matter has been observed in materials that exhibit some structural order. Both liquid crystals (discs), which have no long-range order (with no or very broad Bragg peaks) between the crystal and melt phases, and plastic crystals (spheres, with low melt entropy, and which exhibit strong long-range order), can contain mobile ions with enhanced ionic transport properties in these phases.[6] Liquid-crystalline (LC) columnar assemblies[7,8] based on ionic liquids,[9] doped ionic liquids,[10] liquid crystalline salts,[11] ion-doped plastic crystals,[12−21] and materials with both liquid crystalline and plastic crystal phases,[10] form conductive phases. Enhanced ionic conductivity is observed in membranes containing oriented supramolecular transport channels[22] and in polymer hydrogels.[23] Ion channels form in molecular crystalline soft-solid electrolytes with stoichiometric ratios of organics/salts such as sulfones,[24] diamines,[25] diamides,[26] ethers,[25,27] glymes,[28−32] and dinitriles.[33] Trilithium crystalline LiTFSI/organic complexes,[31] self-assembled phthalocyanines and related compounds,[34] and crown ethers[35−37] also form ion conduction paths in stacked channel structures.

In the case of soft-solid molecular crystals, there are several factors that influence the ionic conductivity. These include: (i) the occurrence of $Li^+$ ion channels with no contact ion pairs between the anions and cations to provide unimpeded directional motion;[38] (ii) more than one channel (2D or 3D migration) preferable to one channel (1D motion); (iii) short $Li^+\cdots Li^+$ hopping distances;[39] and (iv) weak ligand$\cdots Li^+$ interactions with soft ligands (e.g., C≡N) preferable to hard (e.g., ether oxygens).[40] In addition to these considerations, we show here that grain boundaries play an important role. Grain boundaries in molecular crystals are fluidlike and promote $Li^+$ ion diffusion and adhesion between the grains.[38,41]

We investigate the conductive interphases between grains by comparing off-stoichiometric $(Adpn)_{2.3}LiPF_6$ molecular crystals containing excess Adpn, to stoichiometric $(Adpn)_2LiPF_6$ molecular crystals of different sizes (Figure 1). It is important

Received: September 14, 2025
Revised: February 6, 2026
Accepted: February 9, 2026
Published: February 17, 2026

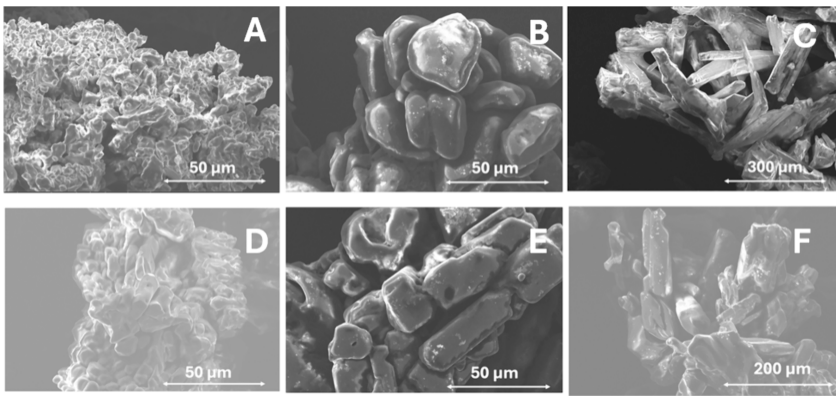


**Figure 1.** SEM images of $(Adpn)_2LiPF_6$ crystals formed by (A) melt crystallization; (B) fast crystallization from acetonitrile (AN); (C) slow crystallization from AN; and SEM images of $(Adpn)_{2.3}LiPF_6$ crystals formed by (D) melt crystallization; (E) fast crystallization from AN; and (F) slow crystallization from AN.

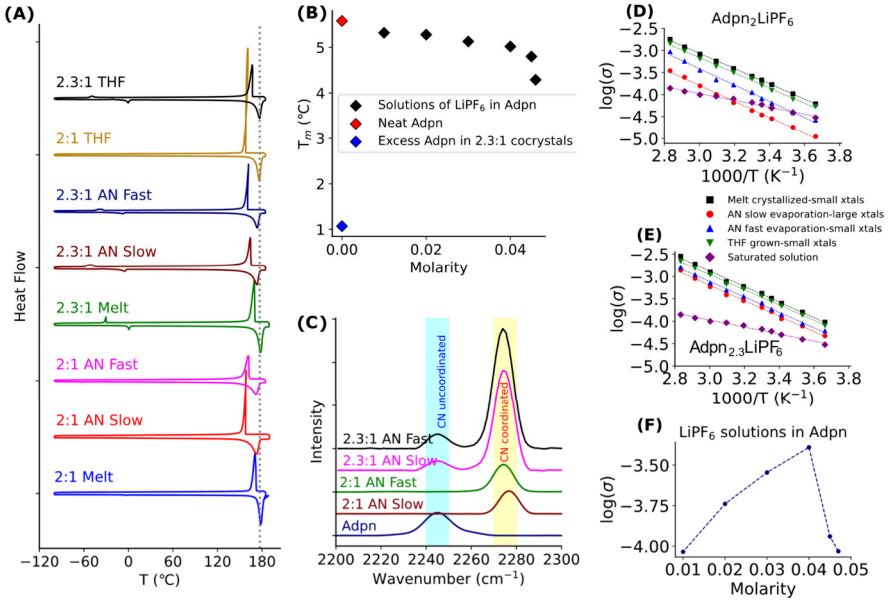


**Figure 2.** (A) DSC data (first cooling/second heating cycles) for $(Adpn)_2LiPF_6$ and $(Adpn)_{2.3}LiPF_6$ crystallized from tetrahydrofuran (THF), quickly and slowly crystallized from acetonitrile (AN), and melt crystallized. No transitions between −100 and +100 °C for $(Adpn)_2LiPF_6$ and small crystallization peaks for $(Adpn)_{2.3}LiPF_6$ around 0 °C (Table 1). In all cases, corresponding enthalpies for melting ($\Delta H_{m2}$) and crystallization ($\Delta H_{c2}$) are same for each sample. (B) $T_m$ of neat Adpn (red), Adpn/$LiPF_6$ solutions up to the saturation limit at 25 °C (black), and Adpn in the nonstoichiometric $(Adpn)_{2.3}LiPF_6$ (blue). (C) Raman spectra of Adpn, $(Adpn)_2LiPF_6$, and $(Adpn)_{2.3}LiPF_6$ stoichiometries of Adpn/$LiPF_6$, crystallized from AN by fast and slow evaporation. All $(Adpn)_2LiPF_6$ peaks have a single peak at 2275 $cm^{-1}$; all $(Adpn)_{2.3}LiPF_6$ peaks have peaks associated with neat and coordinated Adpn. The percentage of free CN, as determined by using the expression (% free CN) = $\frac{I_{\text{free CN}}}{I_{\text{free CN}} + I_{\text{bound}}}$, was 13.0%. Conductivity data from heating cycles for (D) melt- and solution-crystallized $(Adpn)_2LiPF_6$, and saturated solution of $LiPF_6$ in Adpn; (E) melt- and solution-crystallized $(Adpn)_{2.3}LiPF_6$, and a saturated solution of $LiPF_6$ in Adpn; (F) solutions of $LiPF_6$ in Adpn from 0.01 M to solubility limit at 25 °C. Activation energy barriers derived from Arrhenius fit of the datasets in panels (D) and (B) are provided in Table S3 in the SI.

to note that the 15% excess Adpn does not macrophase separate but rather resides in the nanoconfined region between the grains. PXRD data (Figure S1 in the Supporting Information (SI)) are identical for all the samples and agree with PXRD patterns generated from the single crystal XRD of $(Adpn)_2LiPF_6$ with no evidence of Adpn, which, at $T$ = 100 K, is amorphous. Crystal sizes and, thus the amount of grain boundary contribution were varied: Small crystals were obtained by melt crystallization or evaporation from THF and variable size crystals by slower evaporation from AN (see Figure 1, as well as Figures S2 and S3). Thermogravimetric analysis (TGA) data (see Figure S4 and Table S1) show excellent agreement between the experimental and expected weight loss values for the added Adpn. Differential scanning calorimetry data (see Figure 2A and Table 1) show that the width of the melt peaks for the melt-crystallized $(Adpn)_2LiPF_6$, $(Adpn)_{2.3}LiPF_6$ and THF-solution-crystallized $(Adpn)_2LiPF_6$ is narrower, with melt temperatures ($T_m \approx 178$ °C) and melt enthalpies ($\Delta H_m \approx 178$ J/g) that are higher by 5 °C and ∼5 J/g than all the AN solution crystallized samples with $T_m \approx 173$ °C, $\Delta H_m \approx 172$ J/g. These differences indicate more perfect crystal formation in the former case. For the $(Adpn)_{2.3}LiPF_6$ crystals, additional small melting peaks are observed at $T_m$ (Adpn) ≈ −1 to −4.3 °C with small crystallization endotherms (15.8 J/g).

Higher $T_m$ values (Figure 2A, Table 1) can indicate either larger or more perfect crystals. However, here, the melt-


https://doi.org/10.1021/acsmaterialslett.5c01267
ACS Materials Lett. 2026, 8, 764−771

**Table 1. Crystallization Data Derived from DSC Thermograms Shown in Figure 2A**[a]

| Sample, crystallization method | Crystal size ($\mu$m) | Temperature (°C) | | | | | Enthalpy (J/g) | | | |
|---|---|---|---|---|---|---|---|---|---|---|
| | | $T_{m1}$ | $T_{m2}$ | $T_{c1}$ | $T_{c2}$ | $\Delta T_{m2-c2}$ | $\Delta H_{m1}$ | $\Delta H_{m2}$ | $\Delta H_{c1}$ | $\Delta H_{c2}$ |
| **Adpn** | – | 3 | – | −25.2 | – | – | – | – | – | – |
| **$Adpn_2LiPF_6$, melt** | 10−25 | – | 178.1 | – | 170.1 | 8 | – | 175.2 | – | 177.7 |
| **$Adpn_2LiPF_6$, THF** | 25 | – | 177.0 | – | 162.0 | 15 | – | – | – | – |
| **$Adpn_2LiPF_6$, AN fast** | 25 | – | 173.0 | – | 159.3 | 14 | – | 172.6 | – | 171.3 |
| **$Adpn_2LiPF_6$, AN slow** | 100−200 | – | 173.1 | – | 158.8 | 14 | – | 172.7 | – | 171.8 |
| **$Adpn_{2.3}LiPF_6$, melt** | 25 | −1 | 178.0 | −30.4 | 169.0 | 9.2 | 15.7 | 174.2 | 14.5 | 176.3 |
| **$Adpn_{2.3}LiPF_6$, THF** | <25 | – | 177.0 | – | – | – | – | – | – | – |
| **$Adpn_{2.3}LiPF_6$, AN fast** | 25 | −4.3 | 173.2 | −46.8 | 157.3 | 16 | 15.9 | 171.0 | 16.3 | 171.9 |
| **$Adpn_{2.3}LiPF_6$, AN slow** | 100−200 | −4.0 | 173.2 | −43.8 | 155.8 | 18 | 15.9 | 170.7 | 17.0 | 170.3 |

[a]Legend: $T$ = temperature, $\Delta H$ = enthalpy. Subscripts: m = melting, c = crystallization; "1" corresponds to Adpn, "2" corresponds to molecular crystals.

crystallized small crystals (with or without excess Adpn) have higher values of $T_m$ than the similarly small-sized AN solution crystallized sample (with or without excess Adpn). Both the large and small AN solution-crystallized $(Adpn)_2LiPF_6$ and $(Adpn)_{2.3}LiPF_6$ have the same lower $T_m$. Therefore, the crystal size does not account for the 5 °C decrease in $T_m$ values for all the samples crystallized from AN. In addition to the higher $T_m$ for the melt-crystallized samples, the supercooling temperature, i.e., the difference between the melt and crystallization temperature ($\Delta T = T_m - T_c$) is less for the small melt-crystallized $(Adpn)_2LiPF_6$ ($\Delta T$ = 8 °C) than for the AN crystallized $(Adpn)_2LiPF_6$ small and large samples ($\Delta T$ = 14 °C). This suggests that the grains in the melt-crystallized samples have fewer defects than those crystallized from AN, making them easier to recrystallize. Defects may occur in the crystals if a mononitrile like AN occupies sites in the crystal lattice that are not completely replaced by the dinitrile Adpn (creating a hole or CIP), or remain in the crystal lattice, either of which can create defect sites that block $Li^+$ ion migration.

To test this hypothesis, the $(Adpn)_2LiPF_6$ crystals grown via evaporation from THF were compared with crystals grown from AN. $^1$H NMR data of the small (Figure S5A) and large (Figure S5B) $(Adpn)_2LiPF_6$ molecular crystals in $d_6$-DMSO indicate the presence of residual AN. Dissolution of the $(Adpn)_2LiPF_6$ crystals grown from THF in $d_6$-DMSO showed no THF peaks (Figure S5C), i.e., there was no residual THF in the $(Adpn)_2LiPF_6$. These results are consistent with the melting point trends. The high $T_m$ values for the more-perfect co-crystals grown from THF, without trapped THF, were the same as the $(Adpn)_2LiPF_6$ obtained by melt crystallization (177 °C). Less-perfect crystals with defects grown from AN had trapped AN in the grains and $T_m$ values that were lower by 5 °C. The larger mass and size of the THF ligand may be harder to incorporate into the crystal structure than the smaller AN.

To assess the approximate molarity of $LiPF_6$ in the GBs, melt temperatures of Adpn and $LiPF_6$ solutions were measured (Figure 2B) and compared with $T_m$ values for the excess Adpn (~0 °C) in the $(Adpn)_{2.3}LiPF_6$ molecular crystals (Table 1). In the molecular crystals, Adpn melts at lower temperatures (−1 °C to −4.3 °C), compared to neat Adpn (1 to 3 °C), indicating the presence of dissolved $LiPF_6$. In the $LiPF_6$:Adpn solutions (note: the solubility of $LiPF_6$ in Adpn is very low, <0.05 M), the melting points decrease with respect to that of Adpn as the concentration of $LiPF_6$ increases, as expected. However, the melting point of the Adpn in the nonstoichiometric $(Adpn)_{2.3}LiPF_6$ molecular crystal is substantially lower than in the dilute solutions. Since melting point depression is a colligative property, extrapolation of the $T_m$ vs molarity plot, using 0, 0.01, 0.02, 0.03, and 0.04 M, to 1 °C occurred at 0.4 M $LiPF_6$. This result strongly suggests that excess Adpn is more concentrated in the "nanoconfined" swollen grain-boundary regions than in a saturated 0.04 M Adpn solution.

Excess Adpn in different samples, quantified from Raman spectra of "free" (2245 $cm^{-1}$) cyano (C≡N) groups of Adpn and those coordinated with $Li^+$ ions (2275 $cm^{-1}$)[38] confirms that all the $(Adpn)_2LiPF_6$ with stoichiometric amounts of Adpn have a single peak at 2275 $cm^{-1}$ and no Adpn peaks, while all the crystals with excess Adpn, $(Adpn)_{2.3}LiPF_6$, have peaks associated with both the neat and the coordinated Adpn (Figure 2C). Assuming, as was the case for acetonitrile,[42] that the Raman scattering coefficients for the C≡N stretch is the same for the bound and free cyano groups, the percentage of free C≡N groups in the $(Adpn)_{2.3}LiPF_6$ samples is 13%, irrespective of their size.

Conductivity data for stoichiometric $(Adpn)_2LiPF_6$ (heating cycle shown in Figure 2D, cooling cycle shown in Figure S6A) are ranked in the following order: melt-crystallized (10−25 $\mu$m) ≥ THF (25 $\mu$m) > AN fast-crystallized (25 $\mu$m) > AN slow-crystallized (200−300 $\mu$m). Differences between $(Adpn)_2LiPF_6$ involve both the grains and the GBs. The conductivity trends support these effects:

(i) smaller crystals have higher conductivity than larger crystals, since their higher surface areas have higher GB contributions;

(ii) small melt-crystallized $(Adpn)_2LiPF_6$ has higher conductivity than the small solution crystallized $(Adpn)_2LiPF_6$, since GBs fuse during the melt crystallization process;

(iii) Defects in the grains (not GBs) decrease conductivity: $\sigma$ (small melt and THF solution crystallized $(Adpn)_2LiPF_6$ without defects) > $\sigma$ (small AN solution crystallized $(Adpn)_2LiPF_6$). Immobile and low-mobility point-defect obstructions were previously shown to decrease the diffusion constants of $Li^+$ ions.[43]

Although AN could also reside in the GBs, this would result in higher conductivity than for crystals made using THF or melt crystallization, since the conductivity of $LiPF_6$ in AN ($\sigma \approx 5 \times 10^{-2}$ S/cm, 1 M $LiPF_6$ in AN at 25 °C)[44] would, but does not, enhance the conductivity of the AN solution crystallized samples.

For the nonstoichiometric $(Adpn)_{2.3}LiPF_6$, the same conductivity trends (see Figure 2E, as well as Figure S6B) are observed. Further, excess Adpn increases the conductivity of all


https://doi.org/10.1021/acsmaterialslett.5c01267
ACS Materials Lett. 2026, 8, 764−771

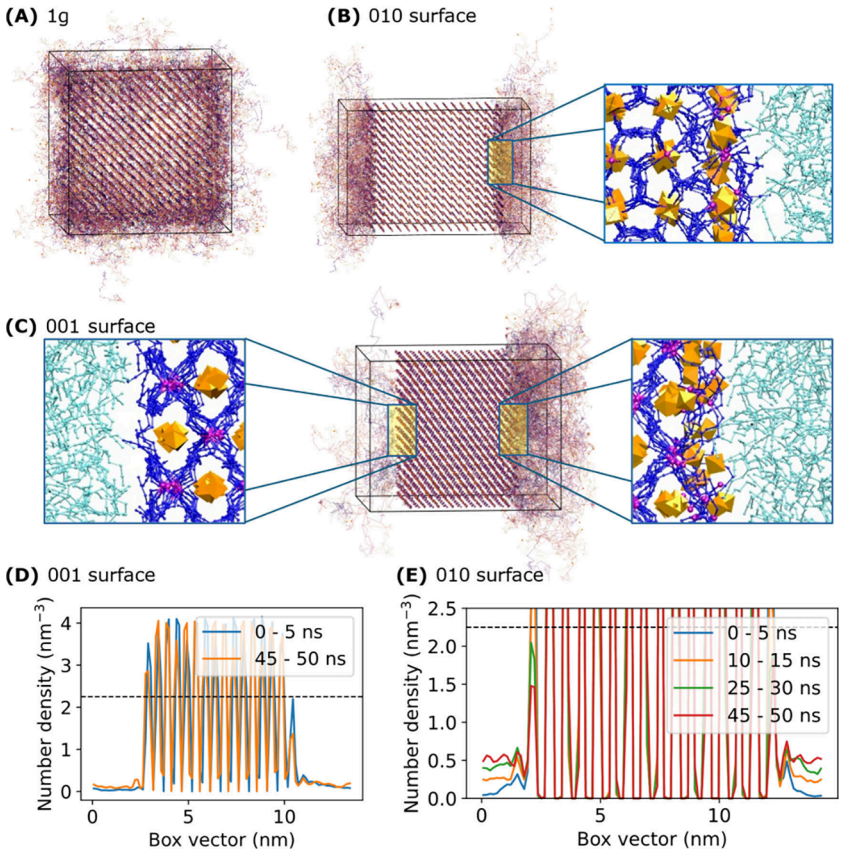


**Figure 3.** Trajectory of $Li^+$ ions in (A) a single large grain (1g), which shows solvation and then exchange of $Li^+$ and $PF_6^-$ ions from all sides of the crystal, while edges and vertices solvate more justifying a rounded (soft edges) appearance of crystals in SEM images; (B) the 010 surface and (C) the 001 models of the grain boundary. The trajectory lines show movement of $Li^+$ and $PF_6^-$ ions from $t = 0$ (dark) to 50 ns (light) lines sampled every 0.5 ns. For the 010 and 001 surfaces, a zoomed-in view of interface is shown (inset), providing a comparative view of surface termination with inherent Adpn (blue balls and sticks, part of crystal stoichiometry) vs excess Adpn (cyan balls and sticks, external solvent molecules). The 010 surface shows consistent solvation and exchange of charge carriers in the GB region. For the 001 surface, only the ions on the right side are solvated and exchanged due to incomplete initial coordination of $Li^+$ ions; the left side remains intact, indicating that completely solvated $Li^+$ ions in the *c*-crystallographic direction do not contribute significantly in generating long-term charge carriers. Number density of $Li^+$ ions across the box in the direction perpendicular to the exposed surface for (D) the 001 surface and (E) the 010 surface.

nonstoichiometrically prepared $(Adpn)_{2.3}LiPF_6$ crystals compared with the corresponding stoichiometrically prepared $(Adpn)_2LiPF_6$, suggesting that the Adpn resides between the grains and increases $Li^+$ ion diffusion. To understand these results, the conductivity of dilute solutions of $LiPF_6$ in Adpn was measured (Figure 2F) and peaked at 0.046 M, ~2 orders of magnitude lower in concentration than the ~1 M typically observed for Li salts in aprotic solvent, due to the low solubility of $LiPF_6$ in Adpn. A saturated solution of $LiPF_6$ in Adpn has a conductivity lower than all the nonstoichiometric $(Adpn)_{2.3}LiPF_6$ and stoichiometric $(Adpn)_2LiPF_6$ cocrystals (except for the AN slow-crystallized sample at $T < 50$ °C). This suggests that the enhanced conductivity for the nonstoichiometric $(Adpn)_{2.3}LiPF_6$ co-crystals is not due to "channels" of dilute $LiPF_6$/Adpn solutions between the crystal grains, which would lead to decreased ionic conductivity.

Furthermore, the activation energies ($E_a$) from temperature-dependent ionic conductivities (Table S3) are almost identical for the stoichiometric crystal (also has GBs) and the nonstoichiometric crystal that contains excess solvent in the GBs. $E_a$ for both stoichiometric and nonstoichiometric molecular crystals ($\Delta E_a \approx 33.5$ kJ/mol) is twice ($\Delta E_a \approx 14.9$ kJ/mol) that of 0.04 M $LiPF_6$ in Adpn; a $\Delta E_a$ typical for LiX in carbonates/ethers ($\Delta E_a \approx 8-15$ kJ/mol). These results, along with the melting point data (Figure 2B), strongly suggest that GBs are complex interfacial regions, where ions move in a nanoconfined space between the grains and can be swollen with excess Adpn. The GB region is more conductive than would be the case for a "channel" of low conductivity 0.04 M $LiPF_6$ in Adpn liquid but less conductive than for a channel of 1 M Adpn if it were soluble at this molarity.

The presence of excess Adpn in the GB region minimizes the difference between the AN solution crystallized small and large crystallized samples) $(Adpn)_{2.3}LiPF_6$ since it serves to better wet and connect the crystal grains, minimizing differences arising from differences in surface area. Other nitriles—succinonitrile (SN) and 1,3,6-hexanetricarbonitrile (HTCN), which are excluded from the crystal lattice to the GBs—also increase the ionic conductivity (Figure S7A and S7B), but can decrease conductivity when viscosity increases.[45] The fluid GB regions make it possible to swell these regions with polymer or polymer gels, decreasing/eliminating the interfacial resistance in polymer/polymer gel and molecular crystal composites.[46]

The effect of grain size on the concentration and dynamics of charge carriers in nanoconfined environments can be modeled using molecular dynamics (MD) simulations. The contributions of grain boundaries (GB) and their thickness to ionic conduction have been shown earlier in a similar class of


https://doi.org/10.1021/acsmaterialslett.5c01267
ACS Materials Lett. 2026, 8, 764−771

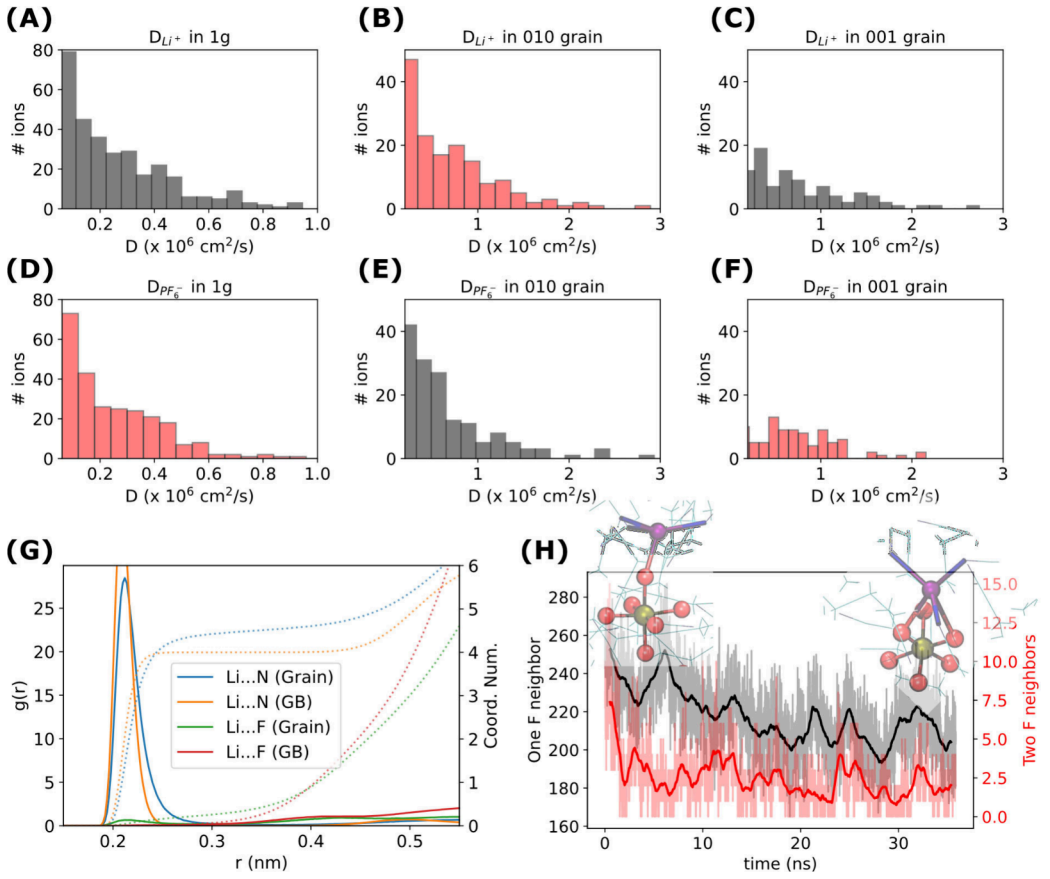


**Figure 4.** Distribution of self-diffusion coefficients for $Li^+$ ions in (A) 1g, (B) 010 grain, (C) 001 grain, and for $PF_6^-$ ions in (D) 1g, (E) 010 grain, (F) 001 grain, only for the charge carriers that are "well-diffusive", defined using slopes MSD vs time plots for each individual charge carrier in Figure S9; (G) Li···N(Adpn) and Li···F($PF_6^-$) radial distribution functions for ions quantified as "in grains" and "in GB", with coordination numbers for $Li^+$ ions with N/F atoms in GB and in grains, calculated from RDFs, particularly showing negligible cation−anion interactions in GB. (H) Number of $Li^+$ ions with one (plateaued to ∼180) or two (plateaued to ∼5) F($PF_6^-$) neighbors in the GB regions. Left inset image shows a sample geometry for short-lived Li···$PF_6$ ion-pair in GB regions, where a $Li^+$ ion (purple) is seen coordinating with one F atom of $PF_6^-$ (red) and three N atoms (blue) from three Adpn molecules. Right inset shows a sample geometry for a longer-lived Li···$PF_6$ ion pair in GB regions, where a $Li^+$ ion is seen coordinating with two F atoms of a single $PF_6^-$ and three N atoms from three Adpn molecules.

electrolytes, using MD simulations, where the $Li^+$ ion motion in the grains was characterized by a subdiffusive hopping mechanism 100 times slower than in the GBs.[38,47] In the current simulations, an atomistic classical force-field[38,47] that was modified to predict diffusion coefficients and transference numbers of $Li^+$ ions in pristine $(Adpn)_2LiPF_6$ and molecular crystals with an excess solvent environment was used. Previous models were extended to increase the grain size (Figure S8a and S8b) and probe the diffusion of ions from different 010 and 001 crystal facets (Figure S8c and S8d). The initial excess volume of Adpn (a minimum of 1 nm on each side) was less than would be needed for the 2.4:1 stoichiometry, which is inaccessible at this scale due to size limits. Figure 3A−C shows the trajectory of $Li^+$ ions in these three models during the time scale of the simulation. Figure 3A shows solvation of $Li^+$ ions at the edges and vertices occurs more than at the 010 or 001 surfaces, suggesting that vertices and edges are important contact points for multiple grains to form viable GB regions. This is consistent with the rounded edges observed in the SEM images of the crystals (Figure 1). Figure 3B shows $Li^+$ trajectories for a supercell exposed in the *b*-crystallographic direction (010 surface). It is important to note that $Li^+$ ions in this channel were previously shown to have the lowest energy barrier for migration.[38] This is due to a 6.2 Å successive distance between $Li^+$ ions in this *b* crystallographic direction, no CIP formation during the transition state (observed from DFT),[38] and the ability to enter/exit the GBs at both ends. Figure 3C shows that, in the *c*-crystallographic (001) direction, $Li^+$ ions are not solvated (left-inset) unless the initial coordination layer with Adpn molecules is half (right-inset). The initial excess solvent layer (2.5 nm) does not populate with charge carriers as well as in the case of the 010 surface. The results for the *c*-crystallographic direction can also be applied to the *a*-crystallographic direction (100 surface), suggesting that only the *b*-crystallographic direction contributes effectively to the GB conduction.

The concentrations of charge carriers in the GB regions are computed using a number density distribution for $Li^+$ ions in each cross-sectional surface slab (Figure 3D and 3E). It is useful to consider the GBs as consisting of regions directly adjacent to the grains (interfacial region) and the region further from this interface, termed GB-solvated regions. The number density distribution shows that for the 001-surface model (Figure 3D), which generates fewer charge carriers to the GBs than the 010 surface, the number of charge carriers remain roughly the same near the start (0−5 ns) of the simulation and near the end (45−50 ns) of the simulation. For the 010 surface, where most of the $Li^+$ ions enter the GB region, a significant continuous growth in


https://doi.org/10.1021/acsmaterialslett.5c01267
ACS Materials Lett. 2026, 8, 764−771

the $Li^+$ number density was observed over the simulation time (Figure 3E). The equilibrium $Li^+$ ion concentration (calculated from the 45−50 ns window) in the GB regions of 010 model was significantly (∼25 times) larger (∼0.5 carriers-$nm^{-3}$, ∼1 M) than in the supersaturated solution of $LiPF_6$ in Adpn (0.04 M). This predicted concentration (1 M) of $Li^+$ ions in the nanoscale GB regions is a similar order of magnitude to its value predicted from extrapolation of the melting point suppression plot (Figure 2B, 0.4 M).

To assess the ionic mobility in the aforementioned model structures, mean-squared displacements (MSDs) of the $Li^+$ and $PF_6^-$ ions were calculated for each individual entity (Figure S9). The MSD vs time plots show that there are more linearly diffusive ("well-diffusive") charge carriers in the 1g model (where all surface considered) than in the 010 and 001 surface models. The distinction further confirms the role of vertices and edges forming fluid grain-boundary regions in the 1g model. The well-diffusive charge carriers are further filtered (where the standard deviation is <1% in their individual slopes for multiple time origins of the MSD vs time plots) to obtain distribution histograms of diffusion coefficients for each model (Figure 4A−F). Roughly 10% (out of 2048 total $Li^+$ and $PF_6^-$ each) of these charge carriers contribute to ion conduction as diffusive charge carriers in the 1g and 010 grain models. This number drops significantly to only ∼4% for the 001 grain surface model case. In comparison with the earlier investigated smaller-sized (higher surface/volume ratio) "two-grain" model[38] (where roughly 40% out of 1000 $Li^+$ and $PF_6^-$ ions each are located in the grain boundaries), the well-diffusive charge carriers are less for the larger-sized (smaller surface/volume ratio) 1g model (only 10%). This agrees with the experimentally observed effect of grain size, where crystals with smaller grains have higher ionic conductivity than those with bigger grains (Figure 2E) due to the increase in charge carriers in the GB for the smaller crystals. The ratio of ionic conductivities for small:big grains is ∼8:1 from experimental data (see Figure 2D, as well as Figure S6A), compared with 8:5 for the 2g (2 small grains):1g (1 big grain) models from simulation data. We can certainly assume that if the concentration of nanoconfined charge carriers changed from 10% to 40% for an 8:5 size ratio in simulations, in experimental crystals, an 8:1 difference can potentially boost the ionic conductivity by 2 orders of magnitude (Figure 2E).

The average diffusion coefficients ($D^+_{Li}$ and $D_{PF_6^-}$), calculated for all ions and then separately for interfacial and GB-solvated regions (Table 2), show that the GB solvated ions are approximately one order more mobile, compared to interfacial ions, in all three models. The average diffusion coefficients for the 010 ions are largest, reaffirming it to be the most potent GB forming facet of the cocrystals. Furthermore, only slightly higher coefficients for the 1g model, compared to the 001 model, are due to the presence of four (two 100 and two 001) low-conductive surfaces out of six and not enough thickness for the excess solvent layers.

We further characterized the nature of $Li^+$ (and $PF_6^-$) ions in the GB regions by calculating the interatomic interactions of $Li^+$ ions as radial distribution functions (RDFs) with F($PF_6^-$) and N(Adpn) for both the grain and GB regions (Figure 4G). In the grains at short distances (∼0.2−0.3 nm), there are negligible $Li^+$···F($PF_6$) interactions, consistent with the crystallographic data. The calculated coordination numbers at the first minima for the grains show negligible contact ion pair (CIP) formation. In the GB region, more CIPs are observed. The calculated coordination numbers at first minima show ∼0.2 ion pairs forming per $Li^+$ ion in the GB regions. To further identify if these ion pairs are long-lived or short-lived, the F atom neighbors around $Li^+$ ions (Figure 4H) are calculated where ∼210 single Li···F bonded short-lived ion pairs are seen with a cutoff of 3.0 Å. Stronger, long-lived ion-pairs (with two Li···F bonds) are observed in only a very small number (∼2−3). Furthermore, for GB $Li^+$ ions, a very similar Li···N RDF and coordination number as for the grains themselves suggests that the $Li^+$ ions in the GB region are predominantly solvated by Adpn. Both of these results indicate that most of the charge carriers in the GB regions are not in CIPs and thus contribute to ionic conductivity without any cross-correlations.

**Table 2. Average Diffusion Coefficients for $Li^+$ and $PF_6^-$ Ions, $D_{Li^+}$ and $D_{PF_6^-}$ for All Well-Diffusive Ions, and Their Averages in Interfacial and GB-Solvated Regions[a]**

| | | $D$ (× $10^6$ $cm^2/s$) | | | | | |
|---|---|---|---|---|---|---|---|
| | | All Ions | | Interfacial ions | | GB solvated ions | |
| Model | | Average | Std. dev | Average | Std. dev | Average | Std. dev |
| **1g** | $Li^+$ | 0.06 | 0.14 | 0.06 | 0.13 | 0.92 | 0.09 |
| | $PF_6^-$ | 0.05 | 0.12 | 0.05 | 0.13 | 0.92 | 0.1 |
| **010** | $Li^+$ | 0.36 | 0.51 | 0.17 | 0.23 | 1.29 | 0.51 |
| | $PF_6^-$ | 0.23 | 0.43 | 0.12 | 0.2 | 1.36 | 0.56 |
| **001** | $Li^+$ | 0.05 | 0.23 | 0.02 | 0.1 | 1.36 | 0.42 |
| | $PF_6^-$ | 0.04 | 0.19 | 0.01 | 0.09 | 1.19 | 0.33 |

[a]For all the well-diffusive ions, the average diffusion coefficients are divided in two boundary limits of $D_{interfacial} < 0.8 \times 10^{-6}$ $cm^2/s < D_{GB\text{-}solvated}$. The interfacial ions, between GB and grains, do not travel far enough in the GB to be a part of nanoconfined region and are also in rapid exchange with the crystal interior bound Adpn molecules. Ions with $D > 0.8 \times 10^{-6}$ $cm^2/s$ are the GB solvated ions, which are part of the nanoconfined solvated region.

Soft-solid molecular crystals consist of grains and fluid grain boundaries that enhance the transport of $Li^+$ ions between the grains. Unlike LICC where (due to resistive grain boundaries) pressure or sintering is required to improve contact between the grains, the soft grain boundaries in molecular crystals can be connected by pressure, melting, or addition of a slight excess of the organic component between the grains. Both experimental ionic conductivities for differently sized and solvated samples and MD simulations show that the total conductivity consists of $Li^+$ ion migration in the grains, as well as in the grain boundaries, processes that may have different activation energies. Since the grain boundaries can be swollen by other low molar mass compounds (e.g., other dinitriles) and/or the fluid GBs can swell a polymer, there is no interfacial resistance between the two components (molecular crystals and polymer or polymer gel). More factors like solvent polarizability, solvent dielectric constant, and ion-pair stabilization energies are to be explored to tailor the GB regions for optimal stability and conductivity.

## ■ ASSOCIATED CONTENT

### Supporting Information

The Supporting Information is available free of charge at https://pubs.acs.org/doi/10.1021/acsmaterialslett.5c01267.

Experimental details (crystal preparation, characterization, thermal and electrochemical measurements, XRD)



https://doi.org/10.1021/acsmaterialslett.5c01267
ACS Materials Lett. 2026, 8, 764−771

and computational details (molecular models, simulations protocols), powdered XRD data, additional SEM images, thermogravimetric analysis data, $^1$H NMR spectra, conductivity data for cooling cycles, table for activation energy barriers, MD model initial structures, and mean-squared displacement vs time plots from MD (PDF)

## AUTHOR INFORMATION


### Corresponding Authors

**Michael J. Zdilla** − *Department of Chemistry, Temple University, Philadelphia, Pennsylvania 19122, United States*; Email: michael.zdilla@temple.edu

**Prabhat Prakash** − *Materials and Process Simulation Center (MSC), California Institute of Technology, Pasadena, California 91125, United States*; orcid.org/0000-0003-1430-2379; Email: pprakash@caltech.edu

**Stephanie L. Wunder** − *Department of Chemistry, Temple University, Philadelphia, Pennsylvania 19122, United States*; orcid.org/0000-0002-7193-4762; Email: slwunder@temple.edu

### Authors

**Shujit Chandra Paul** − *Department of Chemistry, Temple University, Philadelphia, Pennsylvania 19122, United States*

**William A. Goddard, III** − *Materials and Process Simulation Center (MSC), California Institute of Technology, Pasadena, California 91125, United States*; orcid.org/0000-0003-0097-5716

Complete contact information is available at: https://pubs.acs.org/10.1021/acsmaterialslett.5c01267


### Author Contributions

The manuscript was written through contributions of all authors. All authors have given approval to the final version of the manuscript.

### Notes

The authors declare no competing financial interest.

## ACKNOWLEDGMENTS

This work is supported by National Science Foundation Grant (Award No. DMR 2138432), NSF MRI grant (CHE-2215854) and a Department of Energy Grant (Award No. DE-SC0023356). W.A.G. acknowledges support from the Hong Kong Quantum AI Lab, AIR@ InnoHK of the Hong Kong Government. W.A.G. thanks the U.S. National Science Foundation (CBET- 2311117) for support.

## REFERENCES


(1) Yang, H.; Wu, N. Ionic conductivity and ion transport mechanisms of solid-state lithium-ion battery electrolytes: A review. *Energy Sci. Eng.* **2022**, *10*, 1643−1671.

(2) Shahi, K.; Wagner, J. B., Jr. Fast ion transport in silver halide solid solutions and multiphase systems. *Appl. Phys. Lett.* **1980**, *37*, 757−759.

(3) Bocharova, V.; Sokolov, A. P. Perspectives for Polymer Electrolytes: A View from Fundamentals of Ionic Conductivity. *Macromolecules* **2020**, *53*, 4141−4157.

(4) Biao, J.; Han, B.; Cao, Y.; Li, Q.; Zhong, G.; Ma, J.; Chen, L.; Yang, K.; Mi, J.; Deng, Y.; et al. Inhibiting Formation and Reduction of $Li_2CO_3$ to $LiC_x$ at Grain Boundaries in Garnet Electrolytes to Prevent Li Penetration. *Adv. Mater.* **2023**, *35*, No. e2208951.

(5) Zheng, Y.; Yao, Y.; Ou, J.; Li, M.; Luo, D.; Dou, H.; Li, Z.; Amine, K.; Yu, A.; Chen, Z. A review of composite solid-state electrolytes for lithium batteries: fundamentals, key materials and advanced structures. *Chem. Soc. Rev.* **2020**, *49*, 8790−8839.

(6) Dai, Q.; MacFarlane, D. R.; Howlett, P. C.; Forsyth, M. Rapid I-/I-3(−) diffusion in a molecular-plastic-crystal electrolyte for potential application in solid-state photoelectrochemical cells. *Angew. Chem.-Int. Ed.* **2005**, *44*, 313−316.

(7) Kato, T. Self-assembly of phase-segregated liquid crystal structures. *Science* **2002**, *295*, 2414−2418.

(8) Soberats, B.; Yoshio, M.; Ichikawa, T.; Ohno, H.; Kato, T. Zwitterionic liquid crystals as 1D and 3D lithium ion transport media. *J. Mater. Chem. A* **2015**, *3*, 11232−11238.

(9) Yoshio, M.; Mukai, T.; Ohno, H.; Kato, T. One-dimensional ion transport in self-organized columnar ionic liquids. *J. Am. Chem. Soc.* **2004**, *126*, 994−995.

(10) Henderson, W. A.; Passerini, S. Phase behavior of ionic liquid-LiX mixtures: Pyrrolidinium cations and TFSI- anions. *Chem. Mater.* **2004**, *16*, 2881−2885.

(11) Shimura, H.; Yoshio, M.; Hoshino, K.; Mukai, T.; Ohno, H.; Kato, T. Noncovalent approach to one-dimensional ion conductors: Enhancement of ionic conductivities in nanostructured columnar liquid crystals. *J. Am. Chem. Soc.* **2008**, *130*, 1759−1765.

(12) MacFarlane, D. R.; Huang, J. H.; Forsyth, M. Lithium-doped plastic crystal electrolytes exhibiting fast ion conduction for secondary batteries. *Nature* **1999**, *402*, 792−794.

(13) Abouimrane, A.; Abu-Lebdeh, Y.; Alarco, P. J.; Armand, M. Plastic crystal-lithium batteries: An effective ambient temperature all-solid-state power source. *J. Electrochem. Soc.* **2004**, *151*, A1028−A1031.

(14) Zhu, H. J.; MacFarlane, D. R.; Pringle, J. M.; Forsyth, M. Organic Ionic Plastic Crystals as Solid-State Electrolytes. *Trends Chem.* **2019**, *1*, 126−140.

(15) MacFarlane, D. R.; Meakin, P.; Sun, J.; Amini, N.; Forsyth, M. Pyrrolidinium imides: A new family of molten salts and conductive plastic crystal phases. *J. Phys. Chem. B* **1999**, *103*, 4164−4170.

(16) MacFarlane, D. R.; Forsyth, M. Plastic crystal electrolyte materials: New perspectives on solid state ionics. *Adv. Mater.* **2001**, *13*, 957−966.

(17) Pringle, J. M.; Howlett, P. C.; MacFarlane, D. R.; Forsyth, M. Organic ionic plastic crystals: recent advances. *J. Mater. Chem.* **2010**, *20*, 2056−2062.

(18) Jin, L. Y.; Nairn, K. M.; Forsyth, C. M.; Seeber, A. J.; MacFarlane, D. R.; Howlett, P. C.; Forsyth, M.; Pringle, J. M. Structure and Transport Properties of a Plastic Crystal Ion Conductor: Diethyl-(methyl)(isobutyl)phosphonium Hexafluorophosphate. *J. Am. Chem. Soc.* **2012**, *134*, 9688−9697.

(19) Henderson, W. A.; Seo, D. M.; Zhou, Q.; Boyle, P. D.; Shin, J. H.; De Long, H. C.; Trulove, P. C.; Passerini, S. An Alternative Ionic Conductivity Mechanism for Plastic Crystalline Salt-Lithium Salt Electrolyte Mixtures. *Adv. Energy Mater.* **2012**, *2*, 1343−1350.

(20) Jin, L.; Howlett, P. C.; Pringle, J. M.; Janikowski, J.; Armand, M.; MacFarlane, D. R.; Forsyth, M. An organic ionic plastic crystal electrolyte for rate capability and stability of ambient temperature lithium batteries. *Energy Environ. Sci.* **2014**, *7*, 3352−3361.

(21) Forsyth, M.; Chimdi, T.; Seeber, A.; Gunzelmann, D.; Howlett, P. C. Structure and dynamics in an organic ionic plastic crystal, *N*-ethyl-*N*-methyl pyrrolidinium bis(trifluoromethanesulfonyl) amide, mixed with a sodium salt. *J. Mater. Chem. A* **2014**, *2*, 3993−4003.

(22) Beginn, U.; Zipp, G.; Mourran, A.; Walther, P.; Möller, M. Membranes containing oriented supramolecular transport channels. *Adv. Mater.* **2000**, *12*, 513−516.

(23) Wang, K. P.; Yang, Y.; Zhang, Q.; Xiao, Z. Y.; Zong, L. B.; Ichitsubo, T.; Wang, L. Construction of supramolecular polymer hydrogel electrolyte with ionic channels for flexible supercapacitors. *Mater. Chem. Front.* **2021**, *5*, 5106−5114.

(24) Kang, S.; Yang, C.-e.; Jeon, B.; Koo, B.; Hong, S.-T.; Lee, H. A crystalline organic electrolyte for safe, room-temperature operable all-solid-state sodium batteries. *Energy Storage Mater.* **2021**, *39*, 259−264.

(25) Moriya, M. Construction of nanostructures for selective lithium ion conduction using self-assembled molecular arrays in supramolecular solids. *Sci. Technol. Adv. Mater.* **2017**, *18*, 634−643.

(26) Moriya, M.; Nomura, K.; Sakamoto, W.; Yogo, T. Precisely controlled supramolecular ionic conduction paths and their structure-conductivity relationships for lithium ion transport. *CrystEngComm* **2014**, *16*, 10512−10518.
(27) Moriya, M.; Kato, D.; Hayakawa, Y.; Sakamoto, W.; Yogo, T. Crystal structure and solid state ionic conductivity of molecular crystal composed of lithium bis(trifluoromethanesulfonyl)amide and 1,2-dimethoxybenzene in a 1:1 molar ratio. *Solid State Ionics* **2016**, *285*, 29−32.
(28) Zhang, C. H.; Ainsworth, D.; Andreev, Y. G.; Bruce, P. G. Ionic conductivity in the solid glyme complexes $[CH_3O(CH_2CH_2O)_nCH_3]$:$LiAsF_6$ ($n$ = 3,4). *J. Am. Chem. Soc.* **2007**, *129*, 8700−8701.
(29) Zhang, C. H.; Andreev, Y. G.; Bruce, P. G. Crystalline small-molecule electrolytes. *Angew. Chem.-Int. Ed.* **2007**, *46*, 2848−2850.
(30) Zhang, C. H.; Lilley, S. J.; Ainsworth, D.; Staunton, E.; Andreev, Y. G.; Slawin, A. M. Z.; Bruce, P. G. Structure and conductivity of small-molecule electrolytes $[CH_3O(CH_2CH_2O)_nCH_3]$:$LiAsF_6$ ($n$ = 8−12). *Chem. Mater.* **2008**, *20*, 4039−4044.
(31) Moriya, M.; Kitaguchi, H.; Nishibori, E.; Sawa, H.; Sakamoto, W.; Yogo, T. Molecular Ionics in Supramolecular Assemblies with Channel Structures Containing Lithium Ions. *Chem.—Eur. J.* **2012**, *18*, 15305−15309.
(32) Moriya, M.; Kato, D.; Sakamoto, W.; Yogo, T. Structural Design of Ionic Conduction Paths in Molecular Crystals for Selective and Enhanced Lithium Ion Conduction. *Chem.—Eur. J.* **2013**, *19*, 13554−13560.
(33) Tanaka, K.; Tago, Y.; Kondo, M.; Watanabe, Y.; Nishio, K.; Hitosugi, T.; Moriya, M. High Li-Ion Conductivity in $Li\{N(SO_2F)_2\}$-$(NCCH_2CH_2CN)_2$ Molecular Crystal. *Nano Lett.* **2020**, *20*, 8200−8204.
(34) vanNostrum, C. F.; Nolte, R. J. M. Functional supramolecular materials: Self-assembly of phthalocyanines and porphyrazines. *Chem. Commun.* **1996**, 2385−2392.
(35) Percec, V.; Johansson, G.; Heck, J.; Ungarb, G.; Battyb, S. V. Molecular Recognition Directed Self-Assembly of Supramolecular Cylindrical Channel-Like Architectures from 6,7,9,10,12,13,15,16-Octahydro-1,4,7,10,13-Pentaoxabenzocyclopentadecen-2-Ylmethyl 3,4,5-Tris(p-Dodecyloxybenzyl-Oxy)Benzoate. *J. Chem. Soc.-Perkin Trans. 1* **1993**, 1411−1420.
(36) Assouma, C. D.; Crochet, A.; Chérémond, Y.; Giese, B.; Fromm, K. M. Kinetics of Ion Transport through Supramolecular Channels in Single Crystals. *Angew. Chem.-Int. Ed.* **2013**, *52*, 4682−4685.
(37) Nakamura, T.; Akutagawa, T.; Honda, K.; Underhill, A. E.; Coomber, A. T.; Friend, R. H. A molecular metal with ion-conducting channels. *Nature* **1998**, *394*, 159−162.
(38) Prakash, P.; Fall, B.; Aguirre, J.; Sonnenberg, L. A.; Chinnam, P. R.; Chereddy, S.; Dikin, D. A.; Venkatnathan, A.; Wunder, S. L.; Zdilla, M. J. A soft co-crystalline solid electrolyte for lithium-ion batteries. *Nat. Mater.* **2023**, *22*, 627−635.
(39) Paul, S. C.; Zdilla, M. J.; Wunder, S. L. Critical Role of $Li^+\cdots Li^+$ Distance and Anion Restriction in Conductivity and Lithium-Ion Transference Number of Molecular Crystals for Solid State Electrolytes. *Adv. Energy Mater.* **2026**, *16*, No. e03433.
(40) Paul, S. C.; Wunder, S. L.; Zdilla, M. J. Hard−Soft Acid−Base Interactions Control Ionic Conductivity in Molecular-Crystal-Based Electrolytes. *ACS Mater. Lett.* **2026**, *8*, 470.
(41) Katsuragawa, H.; Mori, S.; Tago, Y.; Maeda, S.; Matsuda, S.; Toriu, H.; Nakayama, R.; Kobayashi, S.; Hitosugi, T.; Moriya, M. Molecular Crystalline Electrolyte Based on $Li\{N(SO_2CF_3)_2\}$ and Succinonitrile with Closely Contacted Grain Boundary Interfaces Exhibiting Selective Li-Ion Conductivity and 5 V-Class Electrochemical Stability. *ACS Appl. Energy Mater.* **2025**, *8*, 3599−3605.
(42) Oliver, B. G.; Janz, G. J. Raman spectra of silver nitrate in water-acetonitrile mixtures. *J. Phys. Chem.* **1970**, *74*, 3819−3822.
(43) Malik, R.; Burch, D.; Bazant, M.; Ceder, G. Particle Size Dependence of the Ionic Diffusivity. *Nano Lett.* **2010**, *10*, 4123−4127.
(44) Amara, S.; Toulc'Hoat, J.; Timperman, L.; Biller, A.; Galiano, H.; Marcel, C.; Ledigabel, M.; Anouti, M. Comparative Study of Alkali-Cation-Based ($Li^+$, $Na^+$, $K^+$) Electrolytes in Acetonitrile and Alkylcarbonates. *ChemPhysChem* **2019**, *20*, 581−594.
(45) Chinnam, P. R.; Clymer, R. N.; Jalil, A. A.; Wunder, S. L.; Zdilla, M. J. Bulk-Phase Ion Conduction in Cocrystalline LiCl·*N*,*N*-Dimethylformamide: A New Paradigm for Solid Electrolytes Based upon the Pearson Hard-Soft Acid-Base Concept. *Chem. Mater.* **2015**, *27*, 5479−5482.
(46) Paul, S. C.; Zdilla, M. J.; Wunder, S. L. Composite Electrolytes from Molecular Crystals and Polymers: Absence of Interface Effects. *ChemArxiv* **2025**, DOI: 10.26434/chemrxiv.15000144/v1.
(47) Fall, B.; Sonnenberg, L. A.; Aguirre, J. R.; Paul, S. C.; Prakash, P.; Venkatnathan, A.; Garaga, M. N.; Goddard, W. A., III; Greenbaum, S. G.; Zdilla, M. J.; Wunder, S. L. Effect of Anion Mass on Conductivity and Lithium-Ion Transference Number in the Isomorphic Cocrystals $(Adpn)_2LiXF_6$ (Adpn = Adiponitrile, X = P, As, Sb). *Chem. Mater.* **2025**, *37*, 1798−1809.